

# DC Current Order Optimization Based Strategy for Recovery Performance Improvement of LCC-HVDC Transmission Systems

Renlong Zhu, Xiaoping Zhou, Shuchen Luo, Lerong Hong, Hanhang Yin, and Yifeng Liu

**Abstract**—For the safe and fast recovery of line commutated converter based high-voltage direct current (LCC-HVDC) transmission systems after faults, a DC current order optimization based strategy is proposed. Considering the constraint of electric and control quantities, the DC current order with the maximum active power transfer is calculated by Thevenin equivalent parameters (TEPs) and quasi-state equations of LCC-HVDC transmission systems. Meanwhile, to mitigate the subsequent commutation failures (SCFs) that may come with the fault recovery process, the maximum DC current order that avoids SCFs is calculated through imaginary commutation process. Finally, the minimum value of the two DC current orders is sent to the control system. Simulation results based on PSCAD/EMT-DC show that the proposed strategy mitigates SCFs effectively and exhibits good performance in recovery.

**Index Terms**—Line commutated converter (LCC), high-voltage direct current (HVDC), DC current order calculation, subsequent commutation failure (SCF), recovery.

## I. INTRODUCTION

LINE commutated converter based high-voltage direct current (LCC-HVDC) transmission systems are widely applied owing to the geographical separation of primary energy resources and load centers. To lower the influence of commutation failure (CF), the mechanism and influencing factors of CF have been widely investigated. With control-modification-based methods [1], [2], though the first CF can be mitigated in some degree, it cannot be eliminated under severe faults. Moreover, though the first CF can be eliminated greatly with power-electronics-based methods [3], [4], the

consequent cost of equipment can be significant. Hence, it becomes more imperative to reduce the risk of subsequent commutation failures (SCFs) and optimize the recovery process.

Reference [5] proposes a coordinated marginal current control method to suppress the oscillations after fault. However, the DC current order is calculated by quasi-steady state equation of LCC-HVDC transmission systems and the mitigation of SCFs is not guaranteed. Similarly, [6] and [7] calculate the DC current order via quasi-steady state equation of LCC-HVDC transmission systems, however, the fact that the firing angle (FA) and overlap angle (OA) are different from the rated value is neglected, which would extend the recovery process. Reference [8] proposes an improved control method for SCF mitigation and recovery performance improvement by adaptively modifying the parameter of constant extinction angle (CEA) controller, while the recovery speed is not improved. Additionally, there are also some studies on the optimization of voltage-dependent current order limiter (VDCOL), which aim to reduce the risk of SCFs and improve the recovery performance. However, VDCOL and improved VDCOL are not always effective owing to that the related CF mechanism is lack of interpretation and the DC current order tends to be conservative. Reference [9] proposes an improved current-order limiter control, but the interpretation of physical meaning about CF mechanism is still unclear. Reference [10] estimates the maximum power capacity of LCC-HVDC transmission systems after the fault while considering various constraints based on Thevenin equivalent parameters (TEPs); however, the method is not used in the real-time control of LCC-HVDC transmission systems and the SCFs are not considered.

Thus, a DC current order optimization based strategy for recovery performance improvement of LCC-HVDC transmission systems is proposed, which considers the operating boundary and the SCF mitigation. The first DC current order is calculated by the TEPs and the quasi-steady state equation of LCC-HVDC transmission systems to ensure the maximum active power transfer and the operating boundary. Then, the second DC current order is calculated by imaginary commutation process, which can guarantee the maximum DC current order without SCFs. Finally, the minimum value of the two DC current orders is sent to the control system.

Manuscript received: August 17, 2021; revised: October 11, 2021; accepted: February 8, 2022. Date of CrossCheck: February 8, 2022. Date of online publication: April 22, 2022.

This work was supported by the National Key Research and Development Program of China (No. 2021YFB2400902), the Innovation Young Talents Program of Changsha Science and Technology Bureau (No. kq2107005), and the Postgraduate Scientific Research Innovation Project of Hunan Province (No. QL20210101).

This article is distributed under the terms of the Creative Commons Attribution 4.0 International License (<http://creativecommons.org/licenses/by/4.0/>).

R. Zhu, X. Zhou (corresponding author), L. Hong, H. Yin, and Y. Liu are with the College of Electrical and Information Engineering, Hunan University, Changsha 410082, China (e-mail: 635107372@qq.com; zxp2011@hnu.edu.cn; hlr0908@163.com; 296262037@qq.com; 57340757@qq.com).

S. Luo is with the State Grid Hunan Electric Power Company Limited Economical and Technical Research Institute, Changsha 410011, China (e-mail: 359260010@qq.com).

DOI: 10.35833/MPCE.2021.000569



## II. CALCULATION OF DC CURRENT ORDER

The DC current order in this letter consists of two different parts. The first DC current order  $I_{dord1}$  ensures the maximum active power while keeping certain electric and control quantities within the operation boundary. The second DC current order  $I_{dord2}$  ensures the maximum active power while preventing the LCC-HVDC transmission systems from SCFs.

### A. Calculation of First DC Current Order

The equivalent circuit of a generic LCC-HVDC transmission system is shown in Fig. 1, where  $E$  is the Thevenin equivalent voltage of AC grid;  $R$  and  $X$  are the Thevenin equivalent resistance and Thevenin equivalent reactance of AC grid, respectively;  $P_a$  and  $Q_a$  are the active power and reactive power from LCC-HVDC transmission system to AC grid, respectively;  $Q_c$  is the compensated reactive power;  $\theta$  is the phase angle of the AC bus voltage;  $U$  and  $U_d$  are the AC bus and DC voltages, respectively;  $P_d$  and  $Q_d$  are the active power and reactive power transmitted by the converter station, respectively;  $R_d$  is the DC resistance;  $I_d$  is the DC current; and the subscripts i and r represent the inverter and rectifier, respectively.

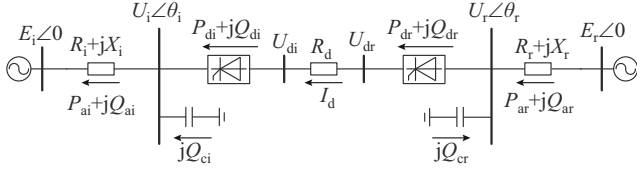


Fig. 1. Equivalent circuit of a generic LCC-HVDC transmission system.

Under the quasi-steady state, the inverter of LCC-HVDC transmission system is controlled by either constant current (CC) controller or CEA controller. The control aims of the CC controller and CEA controller can be described as (1) and (2), respectively.

$$I_d = I_{dord} - I_M \quad (1)$$

$$\gamma_i = \gamma_{iN} \quad (2)$$

where  $\gamma_i$  and  $\gamma_{iN}$  are the extinction angle (EA) and its rated value, respectively;  $I_{dord}$  is the DC current order generated by the control system; and  $I_M$  is the DC current margin between the rectifier and inverter, which is generally  $0.1I_{dN}$  ( $I_{dN}$  is the rated DC current).

The power flow equation of AC grid can be expressed as:

$$\begin{cases} P_{ai} = P_{di} \\ P_{ar} = P_{dr} \\ Q_{ai} = Q_{di} - Q_{ci} \\ Q_{ar} = Q_{dr} - Q_{cr} \end{cases} \quad (3)$$

The compensated reactive power can be calculated as:

$$\begin{cases} Q_{ci} = U_i^2 / X_{ci} \\ Q_{cr} = U_r^2 / X_{cr} \end{cases} \quad (4)$$

where  $X_c$  is the reactance of the reactive power compensator.

The DC power can be calculated as:

$$\begin{cases} P_{di} = U_{di} I_d \\ P_{dr} = U_{dr} I_d \\ Q_{di} = U_{di} I_d \tan \varphi_i \\ Q_{dr} = U_{dr} I_d \tan \varphi_r \end{cases} \quad (5)$$

$$U_{di} = N \left( \frac{3\sqrt{2}}{\pi k_{Tr}} U_i \cos \gamma_i - \frac{3}{\pi} X_{Tr} I_d \right) \quad (6)$$

$$U_{dr} = U_{di} + I_d R_d \quad (7)$$

$$\varphi_i = \arccos \left( \cos \gamma_i - \frac{X_{Tr} I_d}{\sqrt{2} U_i / k_{Tr}} \right) \quad (8)$$

$$\varphi_r = \arccos \left( \cos \alpha_r - \frac{X_{Tr} I_d}{\sqrt{2} U_r / k_{Tr}} \right) \quad (9)$$

$$\alpha_r = \arccos \left( \frac{U_{dr} + \frac{3N}{\pi} X_{Tr} I_d}{\frac{3\sqrt{2} N}{\pi} U_r k_{Tr}} \right) \quad (10)$$

where  $N$  is the number of six-pulse bridges of the converter;  $\varphi$  is the power factor;  $k_{Tr}$  is the transformer ratio; and  $X_{Tr}$  is the equivalent commutation reactance.

The AC power can be calculated as:

$$\begin{cases} P_{ai} = \frac{R_i U_i^2 - U_i E_i (R_i \cos \theta_i - X_i \sin \theta_i)}{R_i^2 + X_i^2} \\ P_{ar} = -\frac{R_r U_r^2 - U_r E_r (R_r \cos \theta_r - X_r \sin \theta_r)}{R_r^2 + X_r^2} \\ Q_{ai} = \frac{X_i U_i^2 - U_i E_i (R_i \sin \theta_i + X_i \cos \theta_i)}{R_i^2 + X_i^2} \\ Q_{ar} = -\frac{X_r U_r^2 - U_r E_r (R_r \sin \theta_r + X_r \cos \theta_r)}{R_r^2 + X_r^2} \end{cases} \quad (11)$$

The AC bus voltage can be calculated as:

$$\begin{cases} U_i = \sqrt{\frac{1}{2} (A_i + B_i)} \\ U_r = \sqrt{\frac{1}{2} (A_r + B_r)} \end{cases} \quad (12)$$

$$A_i = \sqrt{E_i^4 + 4E_i^2 (P_{ai} R_i + Q_{ai} X_i) - 4(P_{ai} X_i - Q_{ai} R_i)^2} \quad (13)$$

$$A_r = \sqrt{E_r^4 - 4E_r^2 (P_{ar} R_r + Q_{ar} X_r) + 4(P_{ar} X_r - Q_{ar} R_r)^2} \quad (14)$$

$$B_i = E_i^2 + 2(P_{ai} R_i + Q_{ai} X_i) \quad (15)$$

$$B_r = E_r^2 - 2(P_{ar} R_r + Q_{ar} X_r) \quad (16)$$

Since we focus on the fault occurs in the inverter-side AC grid, the TEPs of the rectifier-side AC grid is assumed to be constant. Thus, substituting (3)-(10) into (12) leads to:

$$\begin{cases} U_i = f_{U_i}(U_i, \gamma_i, I_d, X_i, R_i, E_i) \\ U_r = f_{U_r}(U_i, U_r, \gamma_i, I_d) \end{cases} \quad (17)$$

where  $f_{U_i}(U_i, \gamma_i, I_d, X_i, R_i, E_i)$  and  $f_{U_r}(U_i, U_r, \gamma_i, I_d)$  are the transcendental equations of  $U_i$  and  $U_r$ , respectively.

Additionally, the following constraints of the LCC-HVDC transmission system should be added:

$$\begin{cases} \alpha_r \geq \alpha_{r,\min} \\ 1.05I_{dN} \geq I_d \geq 0.55I_{dN} \\ 1.1U_{iN} \geq U_i \geq 0.9U_{iN} \\ 1.1U_{rN} \geq U_r \geq 0.9U_{rN} \end{cases} \quad (18)$$

where  $U_{iN}$  and  $U_{rN}$  are the rated values of  $U_i$  and  $U_r$ , respectively; and  $\alpha_{r,\min}$  is the minimum value of FA at the rectifier, which is generally  $5^\circ$ .

For certain TEPs, when the DC current and the EA are controlled at the rated values, the corresponding  $U_i$  and  $U_r$  can be solved by the transcendental equation (17) along with the constraints (18). The operating points with certain TEP can be obtained by setting different DC currents, which range from  $0.55I_{dN}$  to  $1.05I_{dN}$ , and then the first DC current order  $I_{d\text{ord}1}$  with the maximum active power transfer can be identified by comparing the AC active power of different operating points. Thus, a look-up table could be used to calculate  $I_{d\text{ord}1}$  considering that certain TEP correspond to a certain  $I_{d\text{ord}1}$ .

For the application of the proposed strategy, the practicality of TEP estimation method should be firstly evaluated. Both the response speed and the accuracy of the real-time tracking and identification of TEPs during the AC fault transient process can be ensured during the implementation of the proposed strategy. This is firstly because some methodologies have been proposed to obtain and update network pa-

rameters with the data from supervisory control and data acquisition (SCADA) systems and phasor measurement units (PMUs) [11]-[13]. And the TEP estimation method has been recognized as an effective tool for online controller regulation to improve the stability as well [14]-[16], where most of the TEP measurement errors of the above methodologies are within 1%. Secondly, the TEP estimation method has been extended to the control method or online calculation method of HVDC system in recent years. For example, [10] estimated the maximum real-time power capacity of LCC-HVDC transmission systems, which used total least squares to estimate the TEPs. Reference [1] calculated the TEPs by the impedance circle at different time instants, and then selected a FA deduction based on the comparison between pre- and post-fault values of TEPs to reduce the risk of first CF, which requires a quite fast reaction of TEP estimation. Moreover, the method in [1] was verified on real time digital simulator (RTDS). Theoretically, the successful applications of the TEP estimation method into the above-mentioned areas laid a solid basis for using it similarly in this letter. Consequently, the high feasibility of the potential applications of the proposed strategy in real LCC-HVDC projects is indicated.

However, since the first DC current order is calculated by the quasi-steady state equation, the SCFs during the transient process are not fully guaranteed. Therefore, the second DC current order is needed to avoid SCFs.

### B. Calculation of Second DC Current Order

The imaginary commutation process [17] starts at  $t_s$  and ends at  $t_e$ , as shown in Fig. 2, where  $\alpha_i(t_s)$  is the FA at  $t_s$ ;  $\omega$  is the angular frequency;  $\gamma_{i,\text{lm}}(t_e)$  and  $A_{\gamma_{i,\text{lm}}}(t_e)$  are the imaginary EA and imaginary deionization area at  $t_e$ , respectively; and  $A_{\gamma_{iN}}$  is the rated value of the imaginary deionization area.

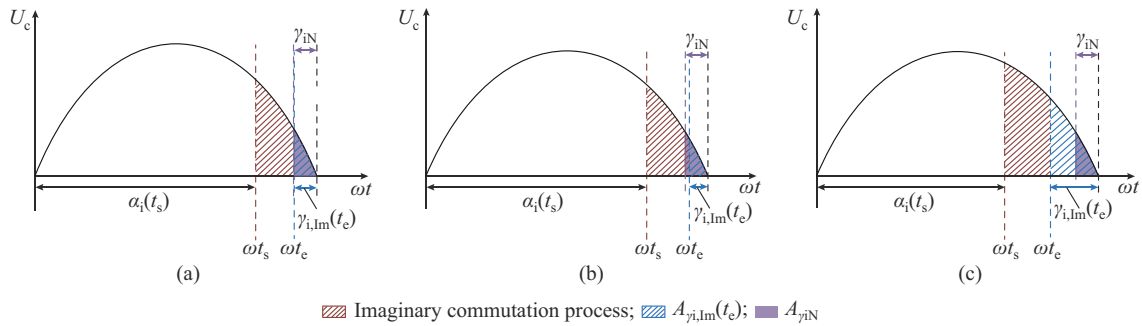


Fig. 2. Imaginary commutation process at different time instants. (a) Normal process. (b) Process after fault and before CF. (c) Recovery process from CF.

During the imaginary commutation process when  $t$  ranges from  $t_s$  to  $t_e$ , the imaginary supply voltage time area can be expressed as:

$$A_{\text{su,lm}}(t) = \sqrt{2} \int_{\alpha_i(t)}^{\alpha_i(t) + \omega(t-t_s)} U_c(t) \sin(\omega t) d\omega t \quad (19)$$

where  $U_c$  is the commutated voltage.

The imaginary demand voltage time area can be expressed as:

$$A_{\text{de,lm}}(t) = X_{ci} (I_d(t_s) + I_d(t)) \quad (20)$$

where  $X_{ci}$  is the equivalent commutated reactance.

Once the inequality (21) holds, the imaginary commutation process is completed, and the corresponding time instant is  $t_e$ .

$$A_{\text{su,lm}}(t) \geq A_{\text{de,lm}}(t) \quad (21)$$

By neglecting the phase shift during the deionization process, the imaginary EA can be calculated as:

$$\gamma_{i,\text{Im}}(t_e) = \pi - \alpha_i(t_s) - \Delta\alpha_i(t_s) - \Delta\varphi(t_e) - \omega(t_e - t_s) \quad (22)$$

where  $\Delta\alpha_i(t_s)$  is the FA shift at  $t_s$ ; and  $\Delta\varphi(t_e)$  is the phase shift at  $t_e$ .

Meanwhile, the imaginary deionization area can be calculated as:

$$A_{\gamma,\text{Im}}(t_e) = \sqrt{2} U_c(t_e) \left(1 - \cos(\gamma_{i,\text{Im}}(t_e))\right) \quad (23)$$

Since the imaginary commutation process can start at any sample time, we can obtain a series of imaginary deionization areas that start at different sample time, which could provide real-time changing data of the imaginary deionization area after fault.

The rated deionization area can be expressed as:

$$A_{\gamma\text{IN}} = \sqrt{2} U_{\text{cN}} (1 - \cos \gamma_{\text{IN}}) \quad (24)$$

where  $U_{\text{cN}}$  is the rated commutated voltage.

For imaginary commutation process with the rated deionization area and the second DC current order, we can obtain:

$$A_{\gamma_i,\text{Im}}(t_e) + A_{\text{de,Im}}(t_e) = A_{\gamma\text{IN}} + A_{\text{de,new}} \quad (25)$$

where  $A_{\text{de,new}}$  is the demand voltage time area with the second DC current order.

Assuming that the DC current variation  $\Delta I_d$  is added to the original DC current when the second DC current order is applied, substituting (20) into (25) yields:

$$A_{\gamma_i,\text{Im}}(t_e) + X_{\text{ci}}(I_d(t_s) + I_d(t_e)) = A_{\gamma\text{IN}} + X_{\text{ci}}(I_d(t_s) + \Delta I_d + I_d(t_e) + \Delta I_d) \quad (26)$$

$\Delta I_d$  can be expressed as:

$$\Delta I_d = \frac{A_{\gamma_i,\text{Im}}(t_e) - A_{\gamma\text{IN}}}{2X_{\text{ci}}} \quad (27)$$

Thus, the second DC current order  $I_{\text{dord2}}$  can be calculated as:

$$I_{\text{dord2}} = I_d + \Delta I_d \quad (28)$$

As observed from Fig. 2(a), when the LCC-HVDC transmission system operates under normal conditions, the commutated voltage and the EA equal the rated values. Therefore, the imaginary deionization area equals the rated value as well, and the second DC current order equals the rated DC current based on (27) and (28). However, after AC fault occurs, due to the decrease of commutated voltage and the increase of DC current, the imaginary deionization area becomes smaller than the rated value, as shown in Fig. 2(b). Thus, the second DC current order tends to drop to mitigate CF or SCFs based on (27) and (28). As observed from Fig. 2 (c), after the first CF, the decrease of FA often exceeds the need due to the CEA control, resulting in the imaginary deionization area always larger than the rated value. Under this condition, the second DC current order is apparently larger than the measured DC current, then setting the calculated second DC current order as the DC current order will accelerate the recovery process and avoid SCFs.

It is worth noting that, the second DC current order can only mitigate SCFs and cannot keep certain electric and control quantities within their boundaries. Thus, the minimum

value of the first DC current order and the second DC current order is selected and sent to the control system. Moreover, to avoid DC current fluctuation during the recovery, the method proposed in [8] is partially adopted, which adaptively modifies the upper and lower limits of the CEA controller. Besides, other EA prediction methods [18]-[20] could be used for the deionization area calculation in the proposed strategy as well.

The block diagrams of control system of the CIGRE HVDC benchmark model (CIGRE control) and the proposed strategy are shown in Figs. 3 and 4, respectively. In Fig. 3,  $I_{\text{dord,input}}$  is the DC current order from higher controller, and ‘‘min in cycle’’ is a module that outputs the minimum value of input in the last 20 ms. Moreover, to avoid the slight fluctuation of  $I_{\text{dord1}}$  and  $I_{\text{dord2}}$  caused by the calculated time-varying TEPs and the minor change of deionization area,  $I_{\text{dord1}}$  and  $I_{\text{dord2}}$  remain unchanged when the change of  $I_{\text{dord1}}$  and  $I_{\text{dord2}}$  are within 0.01 p.u..

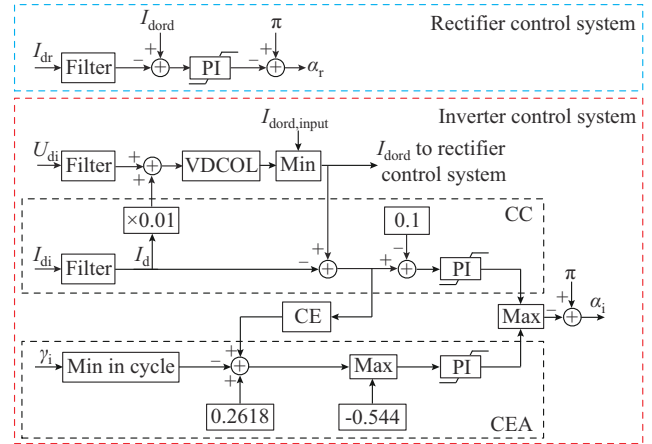


Fig. 3. Block diagram of CIGRE control.

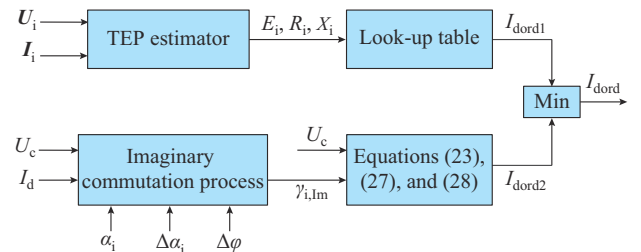


Fig. 4. Block diagram of proposed strategy.

### III. ANALYSIS OF SIMULATION RESULTS

To validate the effectiveness of the proposed strategy, several simulations are performed using the CIGRE control based on PSCAD/EMTDC. The simulation step is 10  $\mu\text{s}$ , and the sampling time and control step are both 100  $\mu\text{s}$ .

#### A. Performance of Proposed Strategy Under AC Faults

In this study, A-G and ABC-G AC faults are applied in a typical case to verify the effectiveness of the proposed strategy in terms of the SCF mitigation. With different grounding inductance  $L_g$ , the faults are applied at the inverter-side AC bus to simulate different fault severity levels. Herein, the initial time of faults varies from 2.000 s to 2.009 s with a step

size of 0.001 s and a fault duration of 0.4 s.

In the simulation of the A-G fault,  $L_f$  varies from 0.2 to 1.2 H. The simulation results of the A-G fault are shown in Fig. 5(a) and (b). As shown in Fig. 5(a), with the CIGRE control, SCFs occur at most of the faults. However, as can be observed from Fig. 5(b), with the proposed strategy, the

SCFs can be mitigated at all fault severity levels. Moreover, when  $L_f=1.1$  H, the first CFs occurring at 2.007 s and 2.008 s are mitigated as well. Besides, the first CF mitigation capability of the proposed strategy can be further investigated with the cooperation of proper FA advancing control.

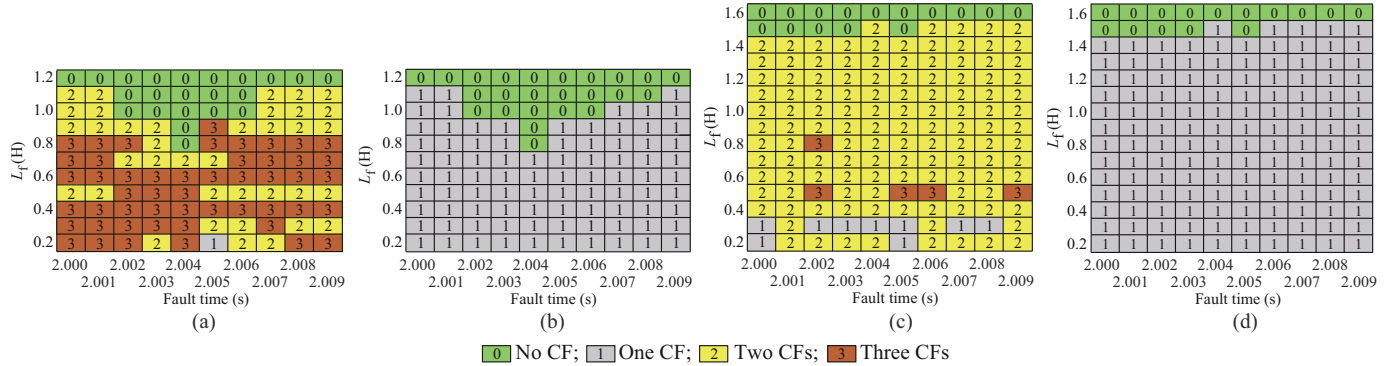


Fig. 5. Simulation results for AC faults with different grounding inductance and different initial time of faults. (a) A-G fault with CIGRE control. (b) A-G fault with proposed strategy. (c) ABC-G fault with CIGRE control. (d) ABC-G fault with proposed strategy.

In the simulation of the ABC-G fault,  $L_f$  varies from 0.2 to 1.6 H. The simulation results of the ABC-G fault are shown in Fig. 5(c) and (d). As shown in Fig. 5(c), with the CIGRE control, the SCFs occur at most of the faults. However, as can be observed from Fig. 5(d), with the proposed strategy, the SCFs

can be mitigated at all fault severity levels.

The simulation results when the ABC-G fault occurs at 2.0 s for a duration of 0.4 s and  $L_f$  of 0.9 H are shown in Fig. 6(a).

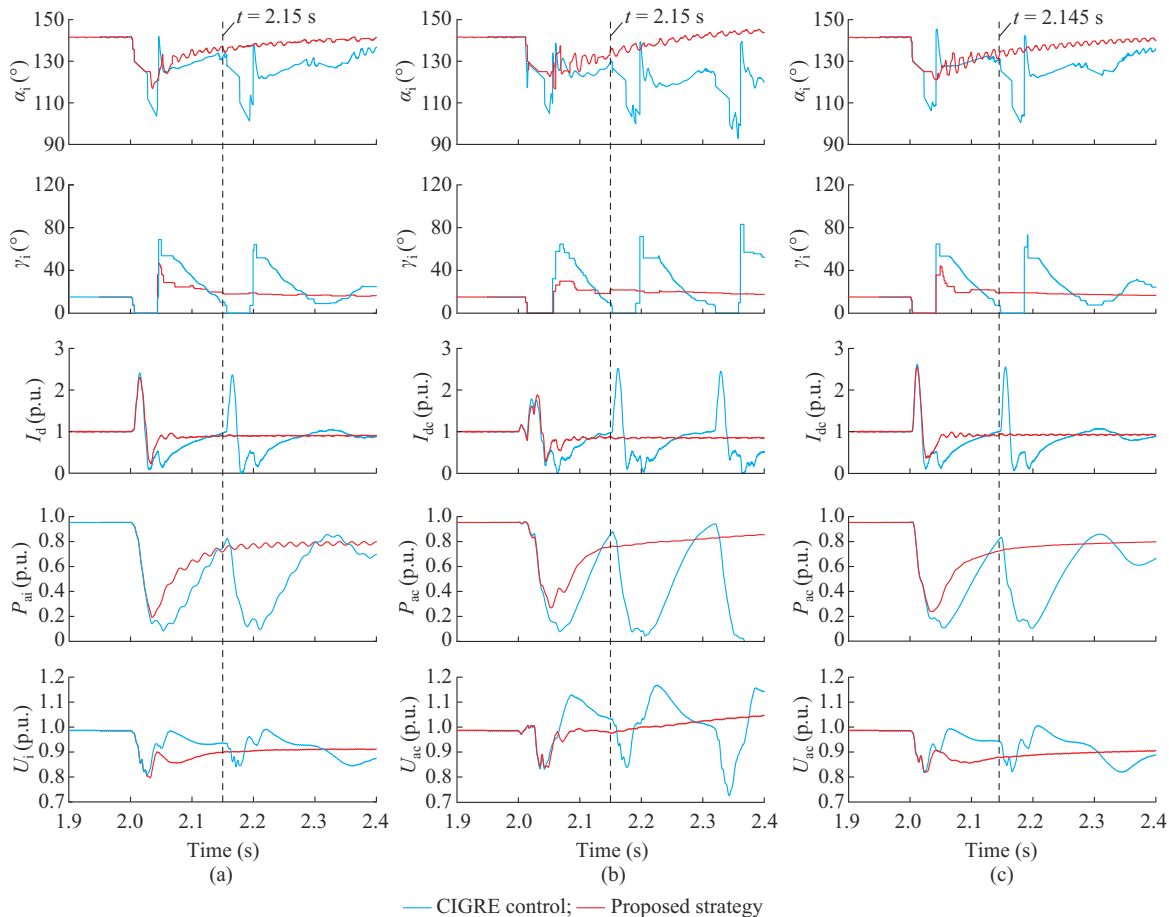


Fig. 6. System response with CIGRE control and proposed strategy under different faults. (a) ABC-G fault. (b) Faults with changing TEI. (c) Faults with changing TE voltage.

As observed from Fig. 6(a), the SCFs cannot be avoided when the CIGRE control is applied, while it can be avoided when using the proposed strategy. Besides, the active power of the proposed strategy is higher than that of the CIGRE control at most of the time. The active power recovers to 0.5 p.u. at 2.113 s with the CIGRE control, while it recovers to 0.5 p.u. at 2.071 s with the proposed strategy. Moreover, the fluctuation is less significant when the proposed strategy is used. Although the operating point of the CIGRE control is better than that of the proposed strategy at 2.15 s since the DC current and AC voltage are higher than those of the proposed strategy. However, with the CIGRE control, the EA is only 10.2° and the FA is smaller than that of the proposed strategy, which means that the LCC-HVDC transmission system has a high risk of CF. Consequently, SCFs occur shortly after 2.15 s. Therefore, it can be concluded that the proposed strategy performs better in terms of SCF mitigation and recovery performance than the CIGRE control.

### B. Performance of Proposed Strategy When TEP Changes

To verify the applicability of the proposed strategy under different kinds of conditions, faults with changing TEPs are applied in the inverter-side AC grid.

Firstly, the TEI is changed from 1.0 p.u. to 1.5 p.u. from 2.0 s to 2.4 s, i.e., the short circuit ratio (SCR) changes from 2.5 to 1.67. As observed from Fig. 6(b), after the SCR decreases, not only the CF occurs three times, but also the system tends to be unstable. This is because the maximum available power (MAP) decreases with the SCR. When the SCR is 1.67, the DC current corresponding to its MAP is about 0.855 p.u.. If the DC current is larger than 0.855 p.u.,  $dP_{dc}/dI_d$  would represent a negative characteristic, which means that the increase of DC current is counterproductive and would make the system unstable. Under this kind of fault, the CIGRE control cannot observe the change of SCR, and cannot produce a logical DC current. Thus, it is difficult for the system to operate at a new stable point. On the contrary, with the proposed strategy, the SCFs are successfully mitigated, the AC voltage stays at 0.9-1.1 p.u. much longer, and the active power recovers faster. Moreover, the system can be stabilized at the new operating point.

Secondly, the TE voltage is changed from 1.0 p.u. to 0.93 p.u. from 2.0 s to 2.4 s, i.e., the SCR changes from 2.5 to 2.16. As observed from Fig. 6(c), although the operating point of the CIGRE control is better than that of the proposed strategy at 2.145 s, the DC current and AC voltage are higher than those of the proposed strategy. However, with the CIGRE control, the EA is only 7.9° and the FA is smaller than that of the proposed strategy, which means that the CF of the LCC-HVDC transmission system is more likely to occur. Consequently, the SCFs occur shortly after 2.145 s. In summary, the proposed strategy performs better in terms of the active power recovery and the SCF mitigation, and it can keep the AC voltage within the limits as much as possible.

## IV. CONCLUSION

In this letter, a recovery strategy for the safe and fast re-

covery of LCC-HVDC transmission systems after faults is proposed, which achieves the SCF mitigation as well. By analyzing the simulation results, it is verified that by using the proposed strategy, the active power can recover fast and the operating point can be kept within the limits as much as possible. Meanwhile, the proposed strategy can mitigate the SCFs effectively under different kinds of fault.

## REFERENCES

- [1] S. Mirsaedi and X. Dong, "An enhanced strategy to inhibit commutation failure in line-commutated converters," *IEEE Transactions on Industrial Electronics*, vol. 67, no. 1, pp. 340-349, Jan. 2020.
- [2] L. Zhang and L. Dofnas, "A novel method to mitigate commutation failures in HVDC systems," in *Proceedings of International Conference on Power System Technology*, Kunming, China, Oct. 2002, pp. 51-56.
- [3] S. Mirsaedi, D. Tzelepis, J. He *et al.*, "A controllable thyristor-based commutation failure inhibitor for LCC-HVDC transmission systems," *IEEE Transactions on Power Electronics*, vol. 36, no. 4, pp. 3781-3792, Apr. 2021.
- [4] Y. Xue, X. Zhang, and C. Yang, "Commutation failure elimination of LCC HVDC systems using thyristor-based controllable capacitors," *IEEE Transactions on Power Delivery*, vol. 33, no. 3, pp. 1448-1458, Jun. 2018.
- [5] J. Xu, T. Lan, S. Liao *et al.*, "A coordinated marginal current control method for LCC-HVDC," *IEEE Transactions on Power Systems*, vol. 34, no. 6, pp. 4569-4582, Nov. 2019.
- [6] J. Wang, M. Huang, C. Fu *et al.*, "A new recovery strategy of HVDC system during AC faults," *IEEE Transactions on Power Delivery*, vol. 34, no. 2, pp. 486-495, Apr. 2019.
- [7] X. Liu, P. Wang, B. Zheng *et al.*, "Mechanism analysis and mitigation measures for continuous commutation failure during the restoration of LCC-HVDC," *Proceedings of the CSEE*, vol. 40, no. 10, pp. 3163-3172, Mar. 2020.
- [8] L. Hong, X. Zhou, Y. Liu *et al.*, "Analysis and improvement of the multiple controller interaction in LCC-HVDC for mitigating repetitive commutation failure," *IEEE Transactions on Power Delivery*, vol. 36, no. 4, pp. 1982-1991, Aug. 2021.
- [9] C. Guo, Y. Liu, C. Zhao *et al.*, "Power component fault detection method and improved current order limiter control for commutation failure mitigation in HVDC," *IEEE Transactions on Power Delivery*, vol. 30, no. 3, pp. 1585-1593, Jun. 2015.
- [10] L. Peng, J. Zhao, Y. Tang *et al.*, "Real-time LCC-HVDC maximum emergency power capacity estimation based on local PMUs," *IEEE Transactions on Power Systems*, vol. 36, no. 2, pp. 1049-1058, Mar. 2021.
- [11] P. Ren, H. Lev-Ari, and A. Abur, "Tracking three-phase untransposed transmission line parameters using synchronized measurements," *IEEE Transactions on Power Systems*, vol. 33, no. 4, pp. 4155-4163, Jul. 2018.
- [12] S. S. Mousavi-Seyedi, F. Aminifar, and S. Afsharinia, "Parameter estimation of multiterminal transmission lines using joint PMU and SCADA data," *IEEE Transactions on Power Delivery*, vol. 30, no. 3, pp. 1077-1085, Jun. 2015.
- [13] X. Zhao, H. Zhou, D. Shi *et al.*, "On-line PMU-based transmission line parameter identification," *CSEE Journal of Power and Energy Systems*, vol. 1, no. 2, pp. 68-74, Jun. 2015.
- [14] A. Ghanem, M. Rashed, M. Sumner *et al.*, "Grid impedance estimation for islanding detection and adaptive control of converters," *IET Power Electronics*, vol. 10, no. 11, pp. 1279-1288, Sept. 2017.
- [15] R. Luhtala, T. Roinila, and T. Messo, "Implementation of real-time impedance-based stability assessment of grid-connected systems using MIMO-identification techniques," *IEEE Transactions on Industry Applications*, vol. 54, no. 5, pp. 5054-5063, Sept. 2018.
- [16] M. K. de Meerendree, E. Prieto-Araujo, K. H. Ahmed *et al.*, "Review of local network impedance estimation techniques," *IEEE Access*, vol. 8, pp. 213647-213661, Nov. 2020.
- [17] R. Zhu, X. Zhou, H. Xia *et al.*, "Commutation failure mitigation method based on imaginary commutation process," *Journal of Modern Power Systems and Clean Energy*, vol. 10, no.5, pp. 1413-1422, Sept. 2022.
- [18] R. Zhu, X. Zhou, H. Xia *et al.*, "A commutation failure prediction and mitigation method," *Journal of Modern Power Systems and Clean En-*

ergy, vol. 10, no.3, pp. 779-787, May 2022.

- [19] L. Liu, S. Lin, P. Sun *et al.*, "A calculation method of pseudo extinction angle for commutation failure mitigation in HVDC," *IEEE Transactions on Power Delivery*, vol. 34, no. 2, pp. 777-779, Apr. 2019.
- [20] J. Wang, Zi. Wang, X. Xuan *et al.*, "Extinction angle control based on predictive calculation and its improvement," *Power System Technology*, vol. 42, no. 12, pp. 3985-3991, Dec. 2018.

**Renlong Zhu** received the B.S. degree from the College of Electrical and Information Engineering, Hunan University, Changsha, China, in 2018. He has been working toward the Ph.D. degree in electrical engineering in the College of Electrical and Information Engineering, Hunan University since 2020. His research interests include modeling and control of line commutated converter based high-voltage direct current (LCC-HVDC) and voltage source converter based high-voltage direct current (VSC-HVDC).

**Xiaoping Zhou** received the B.S., M.S., and Ph.D. degrees from the College of Electrical and Information Engineering, Hunan University, Changsha, China, in 2009, 2013, and 2018, respectively. Currently, he is a full-time Associate Professor in electrical engineering at Hunan University. His research interests include high-voltage direct current (HVDC), power electronics, distributed generation, and microgrid.

**Shuchen Luo** received the B.S. and M.S. degrees from the College of Electrical and Information Engineering, Hunan University, Changsha, China, in

2018 and 2021, respectively. Since 2021, she has been working for State Grid Hunan Electric Power Company Limited Economical and Technical Research Institute, Changsha, China. Her research interests include demand response and control of LCC-HVDC.

**Lerong Hong** received the B.Eng. degree from the College of Electrical and Information Engineering, Hunan University, Changsha, China, in 2016. He has been working toward the Ph.D. degree in electrical engineering in the College of Electrical and Information Engineering, Hunan University. His research interests include HVDC systems and power electronic converters.

**Hanhang Yin** received the B.Eng. degree from the College of Electrical and Information Engineering, Hunan University, Changsha, China, in 2018. She has been working toward the Ph.D. degree in electrical engineering in the College of Electrical and Information Engineering, Hunan University, since 2020. Her research interests include power electronic converter modeling, stability analysis, and modular multilevel converters.

**Yifeng Liu** received the B.S. degree from the College of Electrical and Information Engineering, Hunan University, Changsha, China, in 2016. He has been working toward the Ph.D. degree in electrical engineering in the College of Electrical and Information Engineering, Hunan University, since 2019. His research interests include modeling and control of power electronic converters, distributed generation, and HVDC systems.